Discrete modeling of low-velocity penetration in sand

Jens Kristian Holmen[a,b,*], Lars Olovsson[c], Tore Børvik[a,b]

[a]*Structural Impact Laboratory (SIMLab), Department of Structural Engineering, Norwegian University of Science and Technology (NTNU), NO-7491 Trondheim, Norway*
[b]*Centre for Advanced Structural Analysis (CASA), NTNU, NO-7491, Trondheim, Norway*
[c]*IMPETUS Afea AB, Sördalsvägen 22, 14160, Huddinge, Sweden*

Abstract

In this paper, a discrete particle method was evaluated and used in numerical simulations of low-velocity penetration in sand. Hemispherical, blunt, and ogival-nosed impactors were tested at striking velocities below 5 m/s. The tests were conducted in a dropped-object-rig where the resisting force from the sand was measured continuously during the experiments. This provided a basis for comparison for the simulations. The shapes of the force-penetration depth curves were different for the various impactors, but the ultimate penetration depths were similar in all tests that were done with the same impact velocity. Three-dimensional discrete particle simulations were generally capable of describing the behavior of the sand. However, the peak resisting force was underestimated, which led to a slight overestimation of the ultimate penetration depth. This discrete particle method has previously been evaluated at high impact velocities. The results presented in this study supplement past results and show that the method can also be used to describe the overall response of sand subjected to low-velocity penetration.

Keywords: Experiment, Discrete particle method, Low-velocity penetration, Impact, Granular materials, IMPETUS Afea Solver

1. Introduction

From meteor cratering to pile driving; penetration of granular materials takes place in many situations at different scales and velocities, but it is challenging to model due to its discrete nature. Discrete modeling of granular matter was pioneered by Cundall and Strack [1], and methods that treat each grain of sand or piece of rock as a separate entity have prevailed ever since. The Particle Flow Code (PFC2D/3D) adopts this distinct element method and can be used to simulate the behavior of crushing rocks [2] and sand [3],

*Corresponding author. Tel.: +47 930 45 837
Email address: jens.k.holmen@ntnu.no (Jens Kristian Holmen)

as well as various penetration conditions in granular media [4–6]. Other codes like LIGGGHTS [7, 8] and EDEM [9] are also being used.

A goal of the discrete modeling approach to penetration is to identify the distribution between the energy dissipating mechanisms of inter-particle friction, particle-intruder friction as well as collisional energy dissipation [10–12]. Specifically, the effect of frictional drag on the penetration has attracted interest [10, 13–15]. Grain fracture also dissipates energy in granular materials subjected to high loading rates; especially during high-velocity impact [16–19]. Sophisticated experimental techniques like digital projectile tracking [10], photoelasticity [13] and grain-scale particle tracking [14] have been developed and are being used to study, in situ, the behavior of granular materials. These studies are mainly done by physicists and they deal with, partially, idealized materials to explore the underlying physics of the problem. Thus, their results can be exploited in a variety of applications at several scales. Recent work also utilizes transparent soils to determine in detail the particle-structure interactions during low-velocity penetration [20].

Cratering processes are especially interesting for planetary impact and are studied frequently in the literature by many authors [10–14, 21–24]. The influence of the relationships between impactor density, diameter, and drop-height; soil properties; and boundary configurations on the penetration depth is often investigated. In the widespread cone penetration tests one measures the resistance to penetration while prescribing the velocity during penetration [4–6, 25].

Low-velocity [6] and high-velocity [26] impact penetration in sand were comprehensively reviewed by Iskander et al. [15] and Omidvar et al. [27]. Effects of soil and penetrator properties on, particularly, deep penetration are covered in these reviews. The penetration depths usually increase with increasing nose sharpness while the peak resisting forces are higher for blunt-nosed impactors. Material properties of the impactor are less important at low velocities since it usually remains undamaged.

In the current study we adopt an engineering approach to solve the penetration problem, meaning that the motion of individual sand grains is not measured or studied in the experimental part of the paper. Instead we evaluate the macroscopic response of the sand and compare it to numerical simulations. The results from this work might in the future be applied for instance in onshore and offshore pile driving, in foundation design and for other cases of low-velocity impact into granular materials. Both the finite element method [28, 29] and discrete numerical methods [4, 6] have been used for such purposes in the past.

The discrete particle method (DPM) used in this paper has been implemented in the commercial explicit nonlinear finite element code IMPETUS Afea Solver [30] which is tailor-made for GPU (graphics

processing unit) computing technology and can run large parallel simulations on standard workstations. This particular DPM was originally developed by Olovsson [31] and used to handle the gas-fabric contact issues in airbag-deployment simulations; it is based on a Lagrangian formulation and uses spherical particles that transfer forces through contact and collisions. It has later been considered for several applications, including blast loading [32], combined blast loading and sand impact [33–36], and high-velocity penetration and perforation of sand [37–39]. The main advantages of this DPM are the computational efficiency, so it can be used for relatively large scale engineering problems; a simple and robust contact formulation; and seamless two-way coupling to a complete nonlinear finite element solver. It does, however, neglect physical phenomena like particle crushing, thermal effects in the sand, as well as adhesion. Further, the computational cost is low because the code incorporates only translational degrees of freedom and omits the rotational degrees of freedom which are usually included in other codes. This might affect the shear strength of granular media. However, in densely packed sand, rotation of single sand grains is assumed to be restricted due to friction, and in this study we assume that the possible effects of rotating grains are accounted for in the friction description.

The main results from this study include a series of penetration tests in sand using three different impactor nose shapes. We also implemented a shear-cap parameter that limits the Coulomb friction force in the commercially available DPM that was introduced above. This was done to allow the same set of parameters to be used over a wide range of impact velocities. Lastly, we validated the DPM by simulating penetration tests at various velocities. Until now, the features of this DPM have only been explored for high pressures and high impact velocities, but we show in this work that the method can also describe the overall behavior of low-velocity penetration in sand.

2. Experimental work

2.1. Material description

Sand from *AB Baskarpsand* in Sweden was used in this study. The median grain diameter was 0.95 mm, the moisture content was less than 0.30 % and the compacted density was 1731 kg/m^3. Figure 1 shows the grain size distribution. The sand consisted of 77.1% quartz (SiO_2), 12.5 % alumina (Al_2O_3) and minor fractions of other elements.

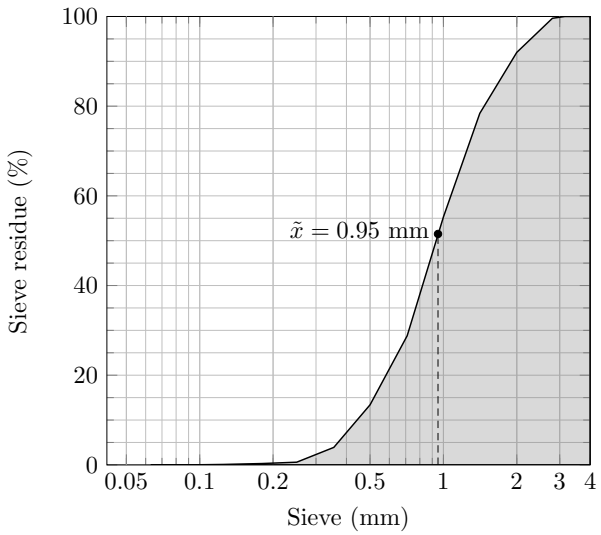

Figure 1: Grading curve for the sand. The median grain diameter $\tilde{x}$ = 0.95 mm is indicated in the figure.

2.2. Test setup and procedure

Figure 2 presents the experimental setup of the impact test. The test machine is an Instron CEAST 9350 dropped-object-rig capable of imparting a maximum kinetic energy of 1800 J. We used impactors with three different nose shapes (Figure 3): a hemispherical-nosed impactor with total mass of 5.0445 kg, a blunt-nosed impactor with total mass of 5.1045 kg, and an ogival-nosed impactor with a total mass of 5.0695 kg. They all have a diameter of 20 mm, and were equipped with a calibrated load cell located approximately 55 mm from the tip. This load cell measured the force with a temporal resolution of 100 kHz. All tests had a measurement duration of 0.1 s giving a total of 10 000 data points for each test. The exact striking velocity was measured by a photoelectric cell just before impact.

Sand was poured into a cylindrical aluminum container with an inner diameter of 123 mm and a height of 350 mm as shown in Figure 4. The side of the container was gently tapped with a rubber hammer to compact the sand before each test and we were attentive to use the same amount of sand every time. This procedure has been applied before and the density in the test specimens was found to be nearly identical to the reported density [38]. All the sand was changed between consecutive tests. We could obtain a maximum penetration depth of 140 mm with the current experimental setup which limited the potential striking velocities. The striker came to a complete stop only due to the resisting force of the sand in all the successful tests.

Five impact tests were conducted with an approximate striking velocity of 2.5 m/s for all nose shapes.

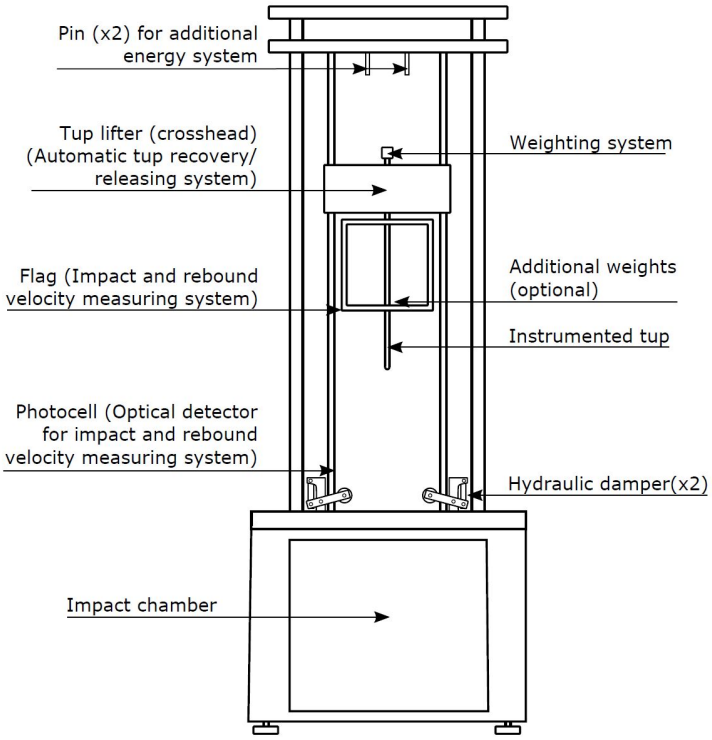

Figure 2: Schematic drawing of the Instron CEAST 9350 dropped-object-rig [40]

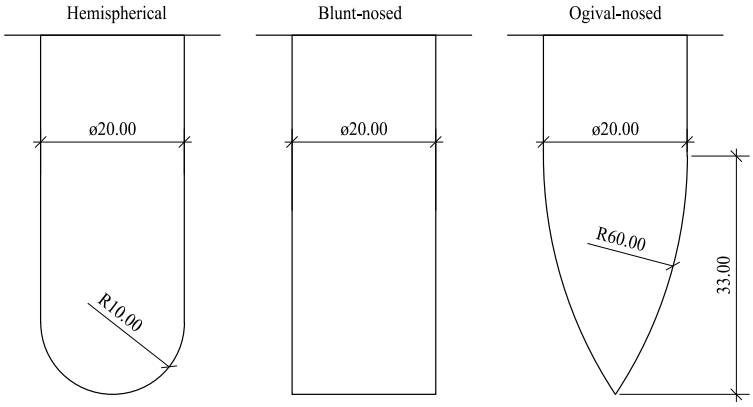

Figure 3: Schematic drawing of the nose shapes considered in this study

An additional five impact tests were done with the hemispherical-nosed impactor at an approximate striking velocity of 5.0 m/s, giving a total of 20 impact tests. The following numerical integration scheme was employed to determine the velocities and displacements from the force measurements:

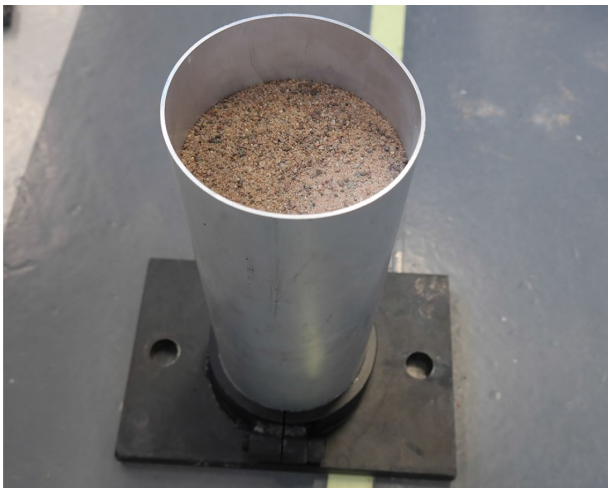

Figure 4: The aluminum tube used to contain the sand in the tests

$$\begin{aligned} v_{n+1} &= v_n - \left(\frac{F_{n+1} + F_n}{2m} - g\right)\Delta t \\ u_{n+1} &= u_n + \left(\frac{v_{n+1} + v_n}{2}\right)\Delta t, \end{aligned} \tag{1}$$

where v is the velocity, u is the displacement, F is the resisting force from the sand on the impactor, m is the total impacting mass, $g = 9.81$ m/s^2 is the gravitational acceleration, and Δt is the sampling time of 0.01 ms. Subscripts $n + 1$ and n denote current and previous values of the variables, respectively. Since the load cell is not located at the tip of the impactor we have to account for the mass below the strain gage to find the resisting force from the sand on the impactor. By using dynamic equilibrium, we obtain the equation for the resisting force as a function of the measured force P as

$$F = P\left(1 + \frac{m_1}{m_2}\right) \tag{2}$$

where m_1 is the mass below the load cell and m_2 is the mass above the load cell ($m = m_1 + m_2$). With the experimental setup used in this work the ratio is $m_1/m_2 \approx 0.02$, and consequently the resisting force is slightly higher than the measured force.

2.3. Experimental results

All the experimental force-penetration depth curves are shown in Figure 5. We identify some experimental scatter, particularly for the hemispherical-nosed impactor, but the overall shape of the curves is similar for replicate tests. Focusing on the tests with an approximate striking velocity of 2.5 m/s and the

hemispherical nose (Figure 5a), we see that the force abruptly increases at initial impact to about 50 N where it remains constant for around 20 mm. At this penetration depth the slope of the curves changes and the force climbs toward its peak that occurs at penetration depths between 70 mm and 80 mm. Halfway to the peak force the slope suddenly increases. The peak is followed by a steep drop in the force. Further penetration results in a second rise in the force before the ultimate penetration depth is reached. In general, the results from the tests with a striking velocity of approximately 5.0 m/s look the same (Figure 5b), but the forces are higher and the displacements are larger.

The tests with the blunt-nosed impactor (Figure 5c) displayed only slight scatter between themselves, but they look different from the hemispherical tests. At initial impact the force rises rapidly to its maximum because of the impactor's flat tip. This takes place at penetration depths lower than 4 mm. A subsequent drop that almost completely unloads the impactor occurs immediately after. Then a plateau with slight slope from a depth of 20 mm to 80 mm precedes a local force maximum just before the ultimate penetration depth.

Figure 5d shows the results from the ogival-nosed impactors. Here the initial impact point was difficult to identify because the ogival shape gave a gradual transition from an unloaded state to a loaded state. At a penetration depth of about 35 mm the initially gentle slope exhibits a distinct kink and in some of the tests this steeper slope lasts until the maximum force is reached at penetration depths around 80 mm. Similar to the hemispherical-nosed impactor the force drops before it increases again right before the ultimate penetration depth. The force in three of the five tests rose slower to the peak, and this peak force occurred at penetration depths between 90 mm and 100 mm. They also had a larger ultimate penetration depth. We believe that these differences can be attributed to the packing of the sand in front of the nose of the impactor.

Table 1 summarizes the experimental results and Figure 6 compares typical force-penetration depth curves for the three nose shapes at an impact velocity of about 2.5 m/s. The divergent is clearly the blunt-nosed impactor for which the force-penetration depth curve has a distinctly different shape than the two other nose-shapes. However, both the average penetration depth and the average work are similar for all nose shapes with the same approximate striking velocity. For the tests with $v_0 \approx 2.5$ m/s, the blunt-nosed impactor experienced the highest peak force from the sand (601 N). This took place immediately after impact. Respective peak forces for the hemispherical and ogival-nosed impactors are 473 N and 453 N and they occur later in the penetration process. We did not see any signs of crushed sand in these tests.

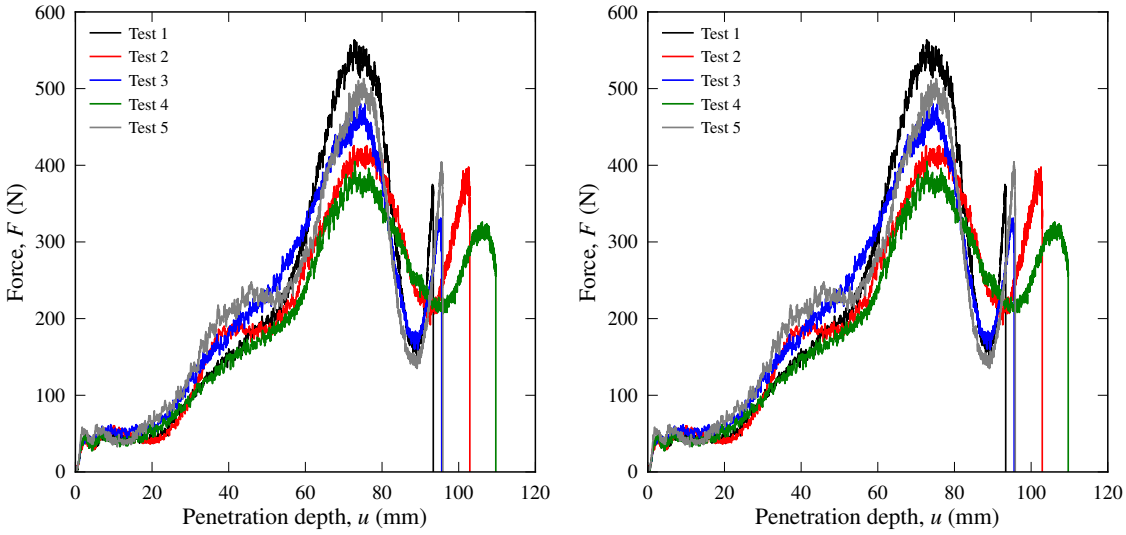

(a) Hemispherical nose, $v_0 \approx 2.5$ m/s

(b) Hemispherical nose, $v_0 \approx 5.0$ m/s

(c) Blunt nose, $v_0 \approx 2.5$ m/s

(d) Ogival nose, $v_0 \approx 2.5$ m/s

Figure 5: Force-penetration depth curves for the various setups. The curves are stopped at maximum displacement. Note that the axes' limits are different.

3. Numerical work

3.1. The discrete particle model

The discrete particle method (DPM) applied in this study uses rigid spherical particles that transfer forces through contact and elastic collisions based on a Lagrangian formulation [33, 34]. Continuum models require constitutive equations for the bulk sand, and, from an impact mechanics perspective, finite elements with element erosion make for instance loose sand ejecta difficult to capture. Similarly, the capability of

Table 1: Number of experimental tests conducted in this study supplemented by some average test data

Nose shape	Number of tests	Avg. striking velocity (m/s)	Avg. maximum penetration depth (mm)	Average maximum force (N)	Average work (Nm)
Hemispherical	5	2.49	100	473	20.6
	5	4.96	134	958	68.6
Blunt	5	2.59	103	601	22.3
Ogival	5	2.63	111	453	23.1

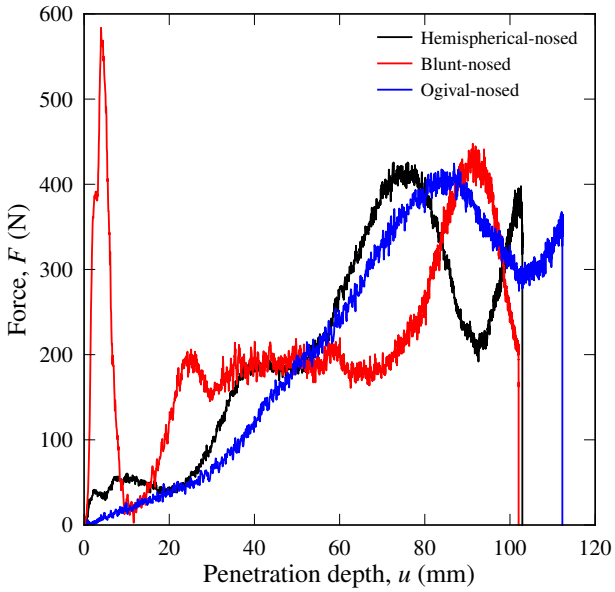

Figure 6: Comparison of representative force-displacement curves for the three different nose shapes with $v_0 \approx 2.5$ m/s

coupled Eulerian-Lagrangian approaches of describing loose sand ejecta and inter-particle contact is limited [41]. They can also suffer from numerical advection errors and contact problems. Two advantages of the discrete particle method we present here are that it needs few input parameters, and that relatively simple assumptions on the particle level are sufficient to capture complicated behavior of the bulk material. Further, for this specific DPM the robust treatment of the interactions between the particles themselves and between the particles and the finite elements allows for a simple and physically clear treatment of for instance the interaction between a deformable structure and sand.

The DPM, which is available in the IMPETUS Afea Solver [30], uses an explicit second-order accurate

central difference time integration scheme, meaning that no equation solving is necessary. It does, however, make the computational effort dependent on the minimum time step, but since particle rotations are neglected in the time integration scheme the model can run large simulation models while keeping the computational time at a reasonable level [33]. It must be noted that neglecting particle rotations means that we cannot capture all the physical mechanisms present in the problem. From a numerical point of view, however, it is an advantage, because rotational degrees of freedom decrease the critical time step significantly. It should be an acceptable simplification as long as the solid-volume fraction is high and we can tune the model parameters to make the aggregate behave correctly [37].

In this study we use the following parts of the rheological model (Figure 7): a normal and a tangential spring with equal stiffness k_s and a frictional element μ_s that scales the tangential inter-particle elastic spring force. Further, friction between the discrete particles and finite elements is controlled by the frictional coefficient μ_{ps}. The rheological model also includes a damping coefficient c_s (usually used for wet sand) and a cut-off value η, or shear cap, which limits the tangential forces between particles (for high velocity impacts). The damping coefficient c_s was not used in this study and the shear cap for the tangential forces η does not affect the results in low-velocity penetration.

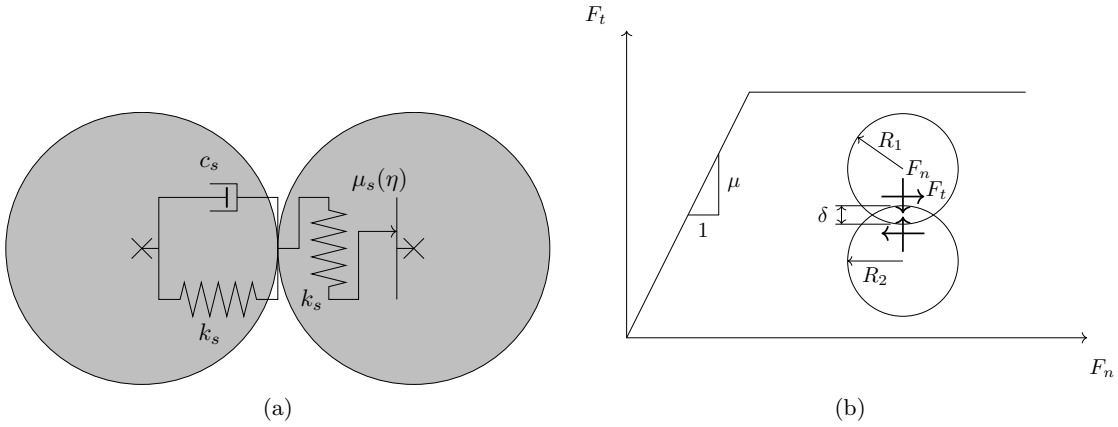

Figure 7: (a) The rheological model for the discrete particles, and (b) the relationship between shear forces and normal forces

We did not see any indication of fracture of the sand grains in the experiments, but when the impact velocity is high, grain fracture can contribute to the energy dissipation. As mentioned, this DPM does not explicitly account for grain fracture, but its effect can be implicitly accounted for in the particle-particle friction μ_s. More advanced simulations of this can for instance be found in Lammi and Vogler [17].

3.2. Numerical models

The numerical simulations were conducted with the IMPETUS Afea Solver [30]. It is a multi-purpose explicit finite element solver that includes the discrete particle method (DPM) described above. All the simulations in this paper were run on a NVIDIA Tesla Kepler K20c GPU mounted in a conventional desktop computer. Figure 8 shows a numerical model in the initial configuration before impact; the sand is represented by particles while the aluminum tube and the impactor are modeled with finite elements. Previous work shows that a particle diameter marginally larger than the median grain diameter in the real sand gives good results [37]. In this work we primarily use a median particle diameter of 1.09 mm, giving 3 200 000 particles in the model. Table 2 lists the parameters that were used in the simulations. We used the compacted sand density ρ_s that was measured in the laboratory and the elastic spring stiffness k_s from a thorough calibration procedure presented elsewhere [33]. The damping coefficient c_s was neglected because friction seems to be the dominating energy dissipating mechanism in dry sand [11], which is also in accordance with prior studies using this DPM [33, 34, 37, 38]. This leaves the friction parameters μ_s and μ_{ps} that were mainly determined by simulating the impacts with the hemispherical-nosed impactor at 2.5 m/s. The blunt-nosed impactor was used adjust the friction parameters further which was especially important to obtain the correct value of μ_{ps}. The simulations indicated that they needed to be significantly higher than what has been used for high velocity impacts in the past [33, 38], which is the reason why a shear cap η was implemented in the model as will be explained in Section 4.3. The model's sensitivity to some of the parameters is presented in Section 3.3.

Table 2: Model constants used in the discrete particle model

ρ_s (kg/m^3)	k_s (N/m)	μ_s	μ_{ps}	c_s	η
1731.0	4.0×10^8	0.5	1.0	0.0	0.0005

An impact simulation consists of two steps: First, we need to compact the sand in an initial analysis. Here a gravitational field is imposed on the model and the sand is given an initial velocity in the same direction as the gravitational acceleration. Second, the positions of the sand particles at the end of the compaction simulation are imported into the main model in which the impactor strikes the sand target. Since neither the impactor nor the aluminum tube showed any signs of deformation in the experiments, we modeled them as rigid bodies. The impactor was prevented from moving in any direction except the impact direction, in the same way as in the tests. The same pre-compaction of the sand was used in all the impact

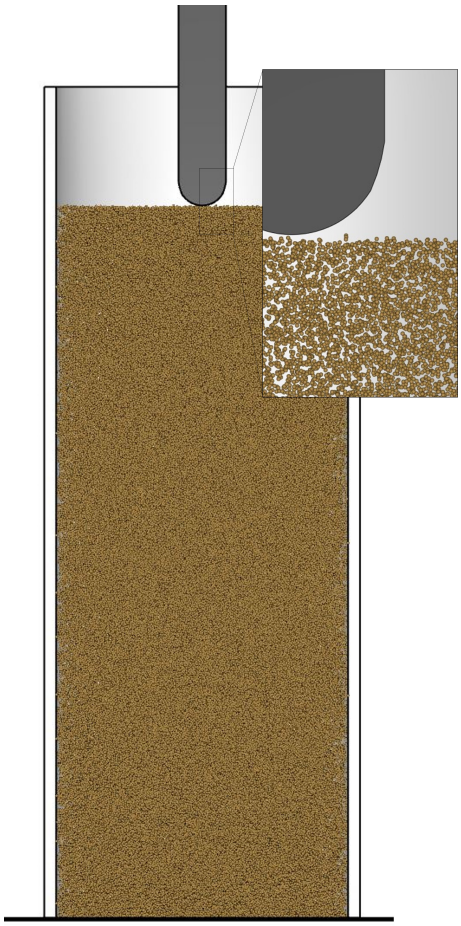

Figure 8: Numerical model of the hemispherical-nosed impactor (the model is sliced in half to improve visualization). There are 3 200 000 particles with a diameter of about 1.09 mm in the model.

simulations, and only the shape, weight, and striking velocity of the impactor were varied.

3.3. Parameter studies

Results from the discrete particle simulations are obviously sensitive to the input parameters. Here, we show how the inter-particle friction μ_s, impactor-particle friction μ_{ps}, and the elastic spring stiffness k_s change the simulation results. We also know that the particle size influences the behavior of the granular assembly: large particles mean high resisting forces. The sensitivity simulations were done with 500 000 particles with a diameter of about 2.0 mm; this dramatically reduces the computational time compared to using 3 200 000 particles. In fact, the computational time is reduced from 110 hours to 12 hours. It means, however, that the ultimate penetration depths are generally underestimated in the sensitivity simulations.

In order to save additional computational time, the hemispherical-nosed impactor impacting at 4.96 m/s

was chosen for the sensitivity study. Figure 9 shows the penetration depth-time curves from a series of simulations. It appears that inter-particle friction, impactor-particle friction and the elastic spring stiffness influence the penetration depth, as expected. Inter-particle friction seems to affect the results more than the two other parameters for this impact configuration. We see that the number of particles also affects the ultimate penetration depth. However, keeping the particle size close to the real grain size makes sense and it also limits the number of adjustable parameters.

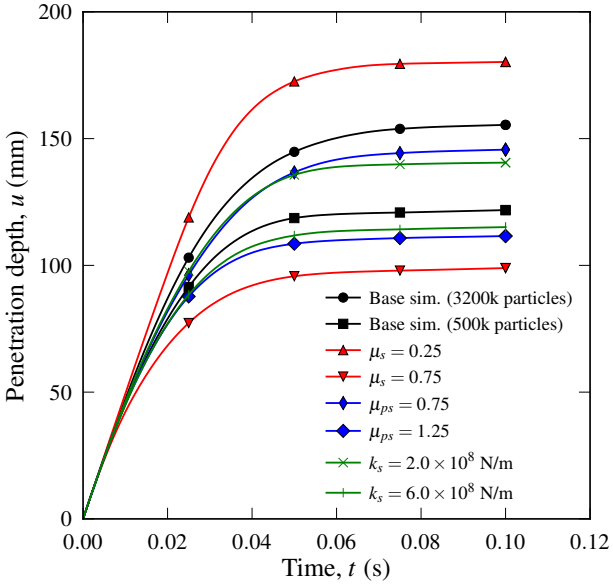

Figure 9: Parametric study for the DPM. The simulations were run with 500 000 particles, $\mu_s = 0.5$, $\mu_p = 1.0$, and $k_s = 4.0 \times 10^8$ unless otherwise stated in the legend.

The diameter of the impactors is rather large (20 mm) compared to the diameter of the aluminum container that holds the sand (123 mm). Due to the extra confinement we can observe resisting forces that are higher, and ultimate penetration depths that are lower, than in corresponding field tests [25]. To assess the influence of the boundary conditions we ran simulations where we varied the diameter of the container. In addition to the standard diameter of 123 mm, diameters of 87 mm, 151 mm, 174 mm and 246 mm were considered. The average particle diameter was kept constant at 2.0 mm which corresponds to 500 000 particles in in the standard container. Figure 10 shows the how the size of the container influences both the force and the penetration depth. We find that the forces go down and the ultimate penetration depth goes up as the size of the container increases.

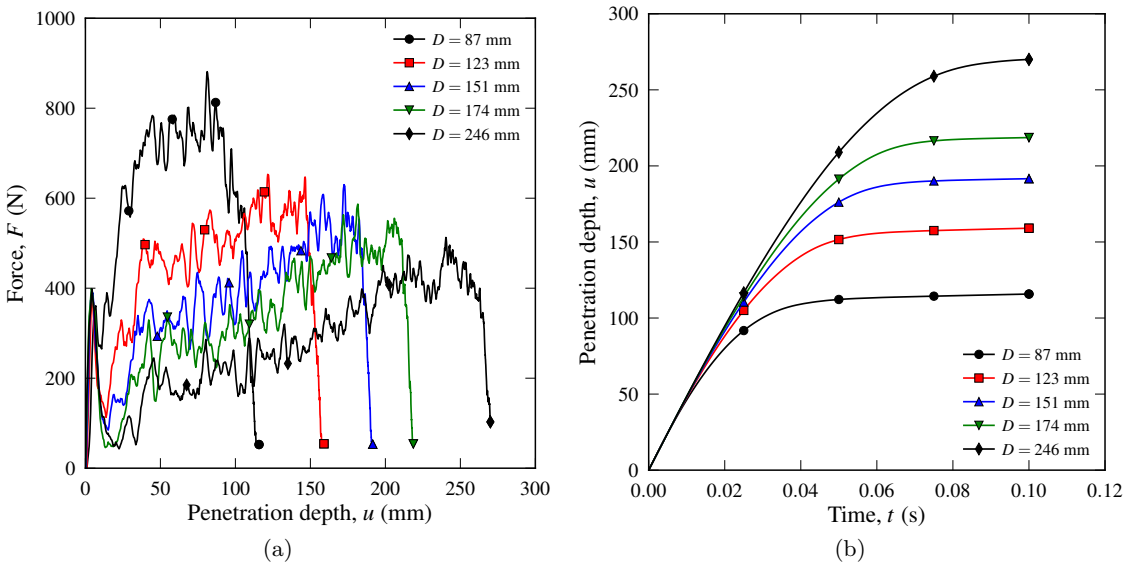

Figure 10: Parametric study on the size of the aluminum container where (a) shows the force versus penetration depth and (b) shows the penetration depth versus time

3.4. Numerical results

We used 3 200 000 particles and the parameters from Table 2 along with rigid boundary conditions and a container diameter of 123 mm in the simulations presented in the following.

Figure 11a and Figure 11b compare the force-penetration depth curves from the numerical simulations to the experiments with the hemispherical-nosed impactor. On average, the force level is captured both for $v_0 \approx 2.5$ m/s and $v_0 \approx 5.0$ m/s, but the simulation overpredicts the resisting force upon impact and underpredicts the force near the ultimate penetration depth. The force from the simulation with the blunt-nosed impactor replicates the experimental data (Figure 11c). The simulation captures the initial force peak immediately after impact, the lower sustained force during most of the penetration, and the increase in force toward the end of the penetration process. Figure 11d shows that the force-penetration depth curve from the numerical simulation of ogival-nosed impact adheres well to the experimental curves, but the predicted peak force is too low.

Table 3 presents data from the simulations and experiments. The peak force was underestimated by around 15 % in all simulations which explains why the final penetration depths were all overestimated. The results confirm that the dissipated energy is about the same in corresponding experiments and simulations.

The contributions to the energy dissipation in the DPM are shown in Figure 12. Initially, we have only kinetic and potential energy of the impactor. Throughout the simulation the impact energy is transferred

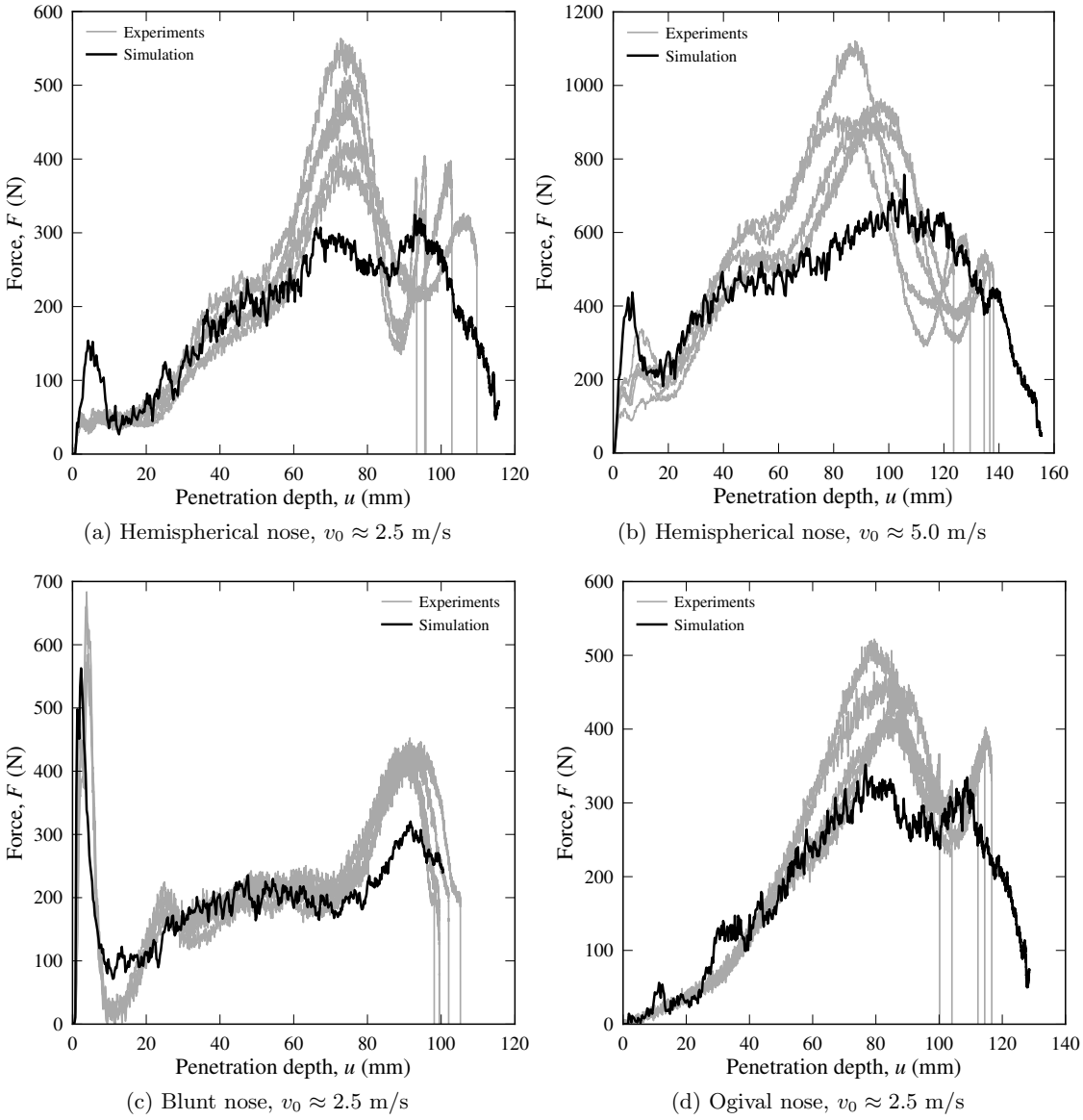

(a) Hemispherical nose, $v_0 \approx 2.5$ m/s

(b) Hemispherical nose, $v_0 \approx 5.0$ m/s

(c) Blunt nose, $v_0 \approx 2.5$ m/s

(d) Ogival nose, $v_0 \approx 2.5$ m/s

Figure 11: Simulated force-penetration depth curves for the various impactors compared to the respective experiments

mainly into internal energy in the sand (inter-particle friction energy), and friction energy between particles and finite elements. Potential and kinetic energy of the sand-particles as they move upwards in the container or jump off the surface as well as contact damping energy are negligible in these simulations. It is clear from Figure 12 that friction between the particles dissipates the most energy, and this is where contributions from any particle fracture would be accounted for.

Table 3: Results from the numerical simulations compared to the average test data from the experiments

Nose shape	Striking velocity (m/s)	Penetration depth			Maximum force			Energy dissipation		
		Exp. (mm)	Sim. (mm)	Dev. (%)	Exp. (N)	Sim. (N)	Dev. (%)	Exp. (Nm)	Sim. (Nm)	Dev. (%)
Hemispherical	2.49	100	115	15.0	473	324	-31.5	20.6	21.4	3.9
	4.96	134	155	13.5	958	757	-20.9	68.6	69.8	1.7
Blunt	2.59	103	116	12.6	601	563	-6.3	22.3	22.5	0.9
Ogival	2.63	111	129	16.2	453	352	-22.3	23.1	23.9	3.5

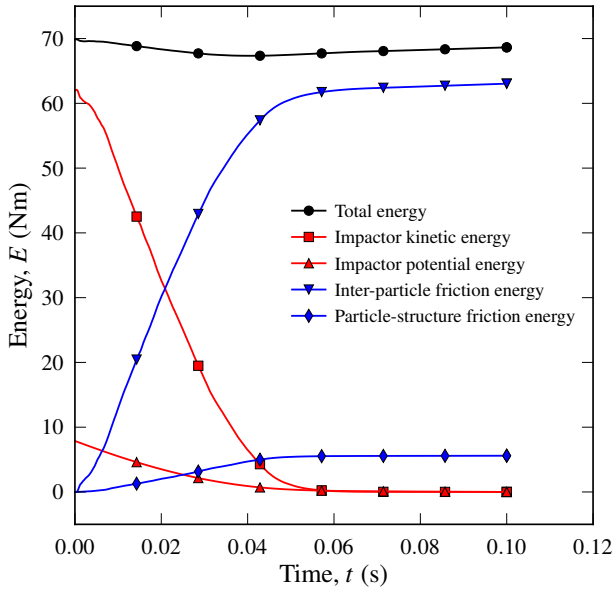

Figure 12: Energy balance for a typical simulation with 500 000 particles

4. Discussion

4.1. Experimental phenomena

Figure 6 illustrates that the sand responds in different ways to penetration by the three different nose shapes. The blunt-nosed impactor experiences large resisting forces during initial penetration because its flat shape does not push the sand away in the lateral direction in the same way as a pointed projectile. When the nose has an ogival shape the resisting force from the sand gradually increases as the impactor penetrates; no abrupt rise in the force was seen for this nose shape. Hemispherical-nosed impactors experience a jump in the force at initial impact, but it stabilizes after about 5 mm of penetration.

Both the hemispherical and ogival-nosed tests exhibit a rather smooth increase in the resisting force toward the peak value. The blunt-nosed impactor, on the other hand, was nearly completely unloaded immediately after the initial force peak before a steep increase in the force took place. Then the force level stabilized until the last local force maximum. We observe a sudden rise in the penetration resistance close to the terminal displacement for all tests regardless of nose shape. This phenomenon has previously been seen for soils subjected to both low velocity and high velocity impact [1]; a possible explanation for this force peak is the transition from inertial resistance to frictional resistance in the sand [42].

Comparing the tests with $v_0 \approx 2.5$ m/s to those with $v_0 \approx 5.0$ m/s for the hemispherical-nosed impactor reveal, as already mentioned, that the overall shape of the force-penetration depth curves remains the same. By doubling the striking velocity, we double the peak force while the ultimate penetration depth increases with only 34 %. Not enough tests were done to draw any further conclusions about the physical reason for this behavior. Thus, an explanation for this response is outside the scope of this study and left for future work.

4.2. On the numerical-simulation results

Previous studies report that impactor-grain frictional effects do not considerably affect the force from the sand on the penetrator if the penetrator is a rather short projectile [15, 43]. Here, we see, numerically, that the impactor-grain friction is important and that the stopping force increases significantly when the impactor-grain friction (μ_{ps}) increases. This is probably because we used a heavy and long rod-like impactor in this study that has a relatively large area on which frictional forces can act.

Figure 13 to Figure 16 show some pictures from simulations and their positions on the corresponding force-penetration depth curves. We see more sand ejecta and larger crater formation when the striking velocity is high (compare Figure 13 to Figure 14). The amount of ejecta and cratering is also nose-shape dependent: both are more pronounced for the blunt (Figure 15) than for the ogival-nosed impactor (Figure 16). We also see from these figures that the peak force for the blunt-nosed impactor happens before any lateral displacement of sand has taken place, meaning that the peak force is probably independent of impactor-grain friction for this nose-shape. Further, the extent of lateral displacement of particles is approximately the same for the all nose shapes. An interesting observation is also that the friction causes the impactor to drag the adjacent particles along with it during the penetration so that the upper layer of the sand has no accumulated lateral displacement toward the end of the simulation.

The simulations capture, with reasonable accuracy, the rise and fall in penetration resistance close to

the ultimate penetration depth, particularly for the blunt and ogival-nosed impactors. Although the behavior was not perfectly reproduced, the average dissipated energy was decently predicted.

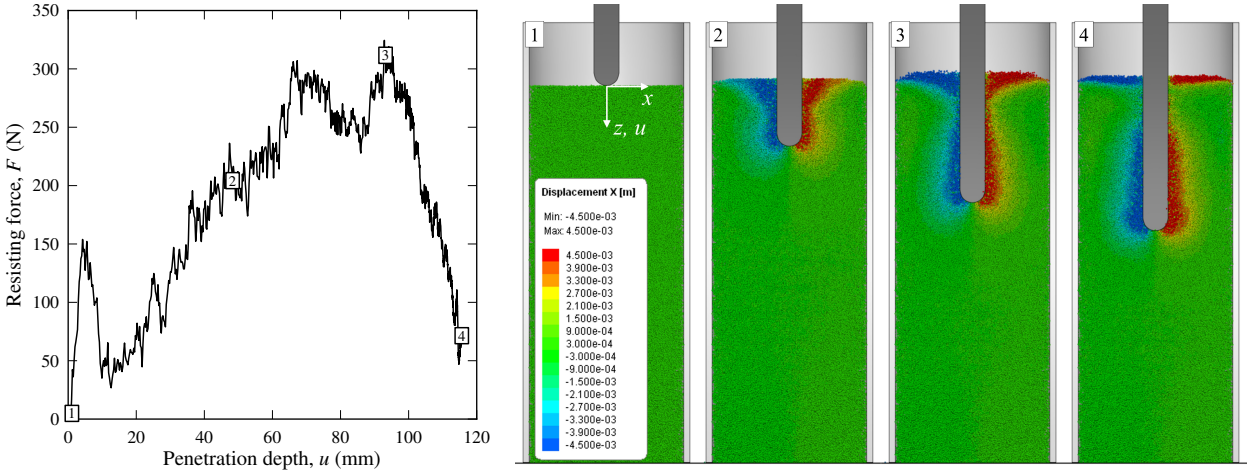

Figure 13: Force-penetration depth synchronized against lateral displacement of the grains for the hemispherical-nosed impactor at $v_0 \approx 2.5$ m/s

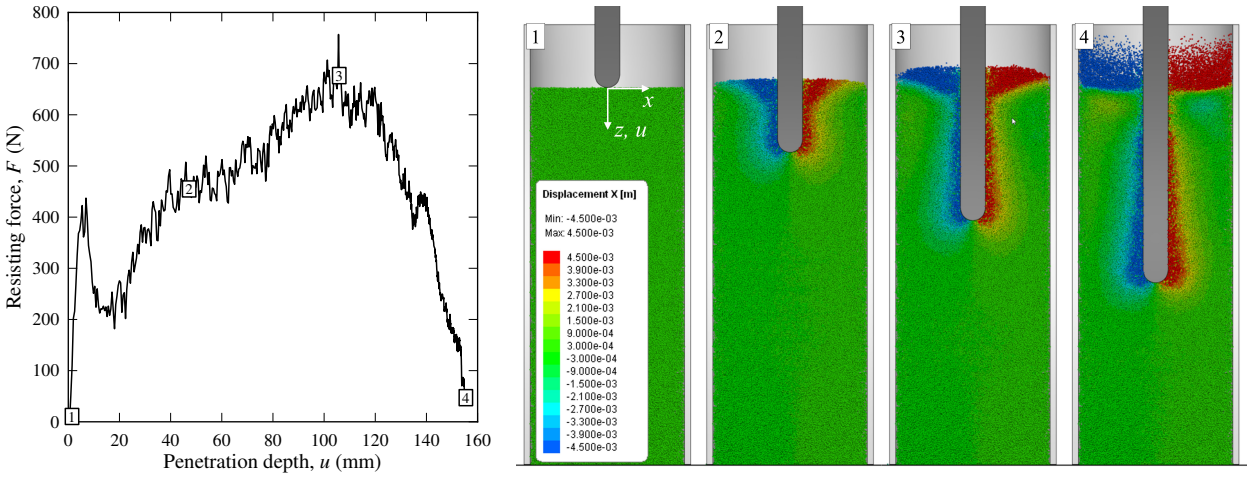

Figure 14: Force-penetration depth synchronized against lateral displacement of the grains for the hemispherical-nosed impactor at $v_0 \approx 5.0$ m/s

4.3. Low versus high-velocity penetration

To illustrate the capability of this DPM to describe impact in sand at both low and high pressures, the same set of parameters that was used in Section 3.2 for striking velocities of less than 5 m/s was used to simulate perforation tests with striking velocities between 150 m/s and 360 m/s. The tangential force cut-off,

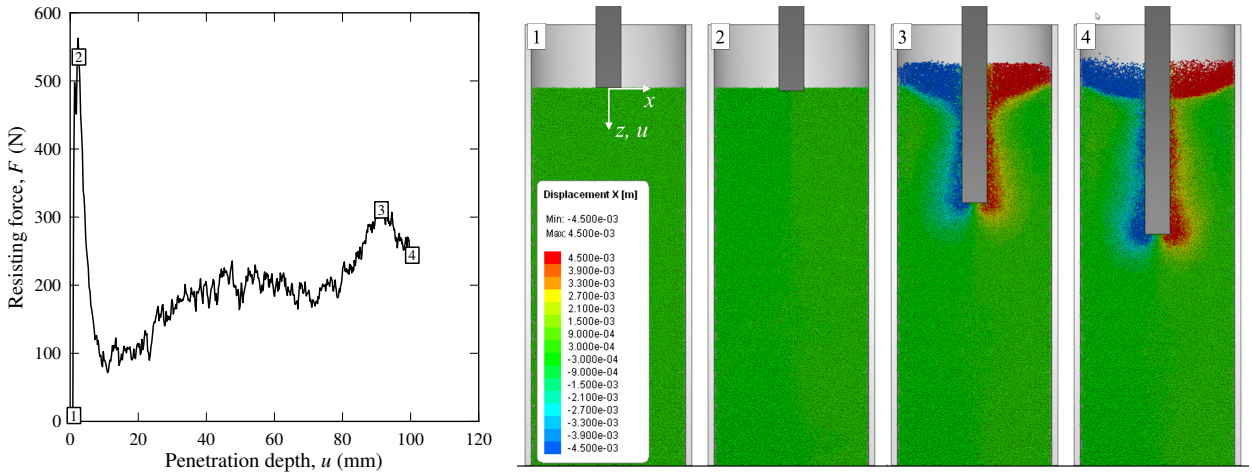

Figure 15: Force-penetration depth synchronized against lateral displacement of the grains for the blunt-nosed impactor at $v_0 \approx 2.5$ m/s

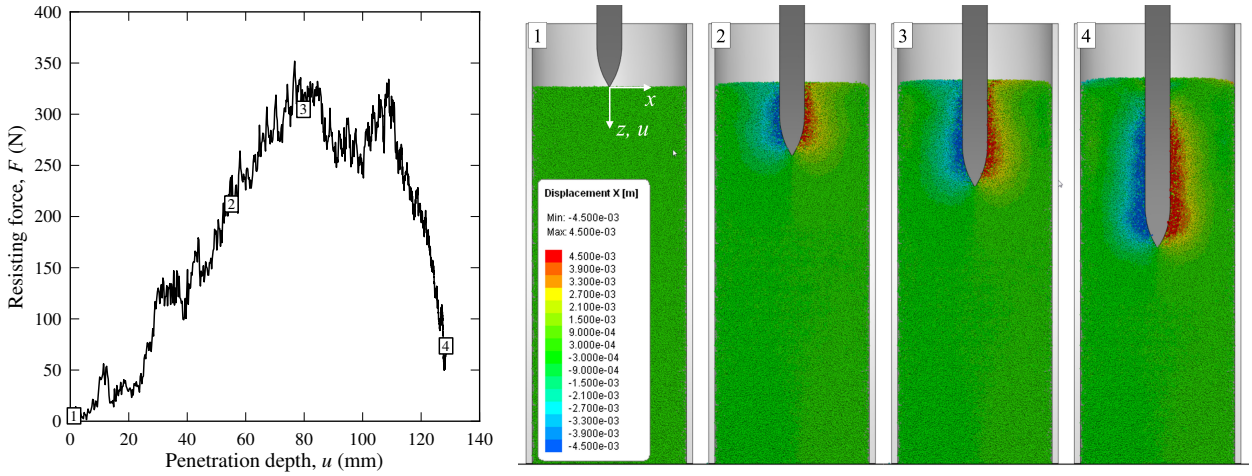

Figure 16: Force-penetration depth synchronized against lateral displacement of the grains for the ogival-nosed impactor at $v_0 \approx 2.5$ m/s

or shear cap (η), now becomes important. This parameter does not influence the results at low velocities, but at high velocities it is crucial in order to obtain good results.

The so-called shear cap works by limiting the tangential forces from above. It allows for continued relative deformation without increasing the resisting forces between the particles. For inter-particle contact the following applies:

$$F_t = \mu_s k_s \min\left(\delta, \eta\left(R_1 + R_2\right)\right) \tag{3}$$

where F_t is the shear force, μ_s is the inter-particle friction coefficient, k_s is the inter-particle stiffness, δ is the contact penetration, η is the dimensionless shear-cap coefficient, while R_1 and R_2 are the radii of the particles in contact. The implication of introducing the shear cap is that the Coulomb friction law is valid only until a certain contact force in the normal direction

$$F_n = F_{\max} = k_s \eta (R_1 + R_2) \tag{4}$$

The same $F_{\max}$ applies in the particle-structure impact. It transpires that the shear force rises until the normal force F_n reaches $F_{\max}$. The shear cap ensures sufficient friction at low pressures while giving reasonable results at high pressures.

A steel sphere with a diameter of 10 mm was fired by a gas gun toward a 50 mm thick sand slab contained in a purpose-made steel box. Holes were drilled in the box and they were covered by 0.1 mm thick domestic aluminum foil to allow for perforation by the steel sphere. We optically measured the striking and the residual velocities with a high-speed camera; further details regarding the experiments are given in Ref. [38]. Figure 17 shows the model of the sand slab that was made in IMPETUS Afea Solver and also the residual velocity as a function of striking velocity compared to the tests. These simulations used 2 650 000 particles, meaning that the particle diameter was approximately 1.09 mm, i.e., about the same as in the main study in this paper. The predicted residual velocities for striking velocities from 100 m/s to 400 m/s are close to the experiments, especially for $\eta = 0.0005$. This shows that the DPM gives reasonable results for higher velocities too. We further see that the value of η affects the results in the following way: higher η gives higher perforation resistance and vice versa. Figure 18 illustrates the behavior of the numerical model compared to an experiment.

5. Concluding remarks

The experimental tests in this paper showed that the shape of the force-penetration depth curves changes dramatically by changing the impactor nose shape. Blunt-nosed impactors have a force peak almost instantaneously after penetration before nearly complete unloading takes place. Hemispherical and ogival-nosed impactors display a gradual increase to the peak force that comes toward the end of the penetration process. For the tests with matching impact velocities the ultimate penetration depths were almost the same regardless of nose-shape. Further, the behavior of the sand, particularly for the ogival-nosed impactor, seems to be determined by the degree of compaction. However, no systematic study of this was done in this paper.

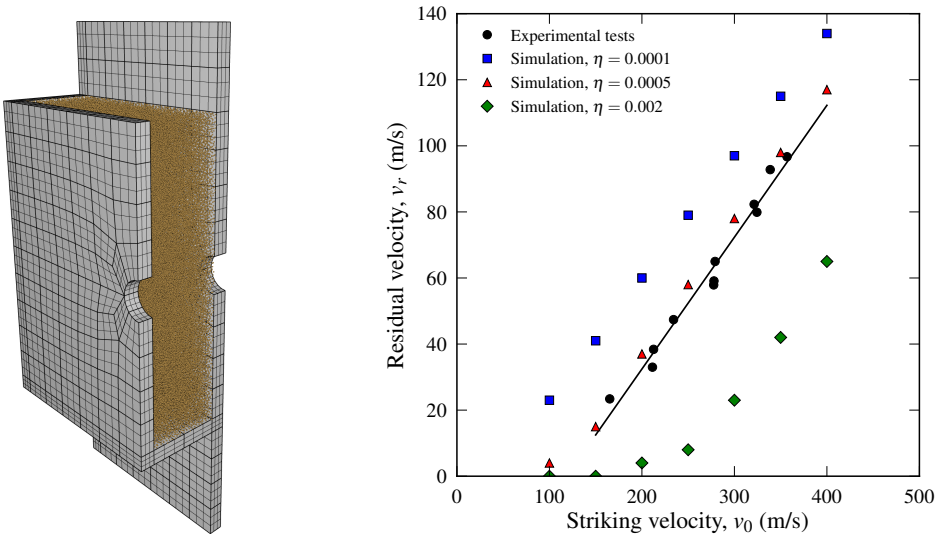

Figure 17: (a) Geometry, and (b) results from simulations with the DPM for perforation tests at high velocities. There are 2 650 000 particles with a diameter of about 1.09 mm in the model.

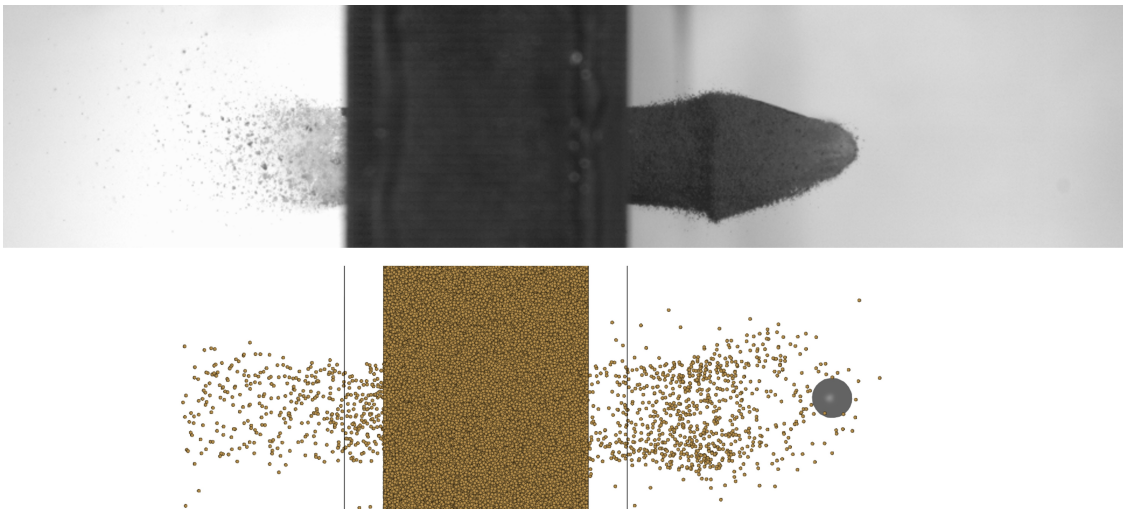

Figure 18: Visual comparison of an experiment (v_0 = 279.1 m/s, v_r = 65.0 m/s) and a simulation (v_0 = 278.2 m/s, v_r = 69.2 m/s) of high-velocity impact

Numerical simulations with a discrete particle method (DPM) were in general able to describe the behavior of the sand during penetration although the peak forces were underestimated by about 15 % and the penetration depths were slightly overestimated. The results presented in this work suggests that this DPM can be used in simulations of low-velocity penetration. And although it has already been explored for used in a range of applications, e.g., low and high velocity penetration and perforation, blast loading,

drilling and mine blasts of buried charges, it needs further development and validation.

Acknowledgment

This research was supported financially by CASA, a Centre for Research-based Innovation, at the Norwegian University of Science and Technology (NTNU).

References

[1] Cundall PA, Strack ODL. A discrete numerical model for granular assemblies. Géotechnique 1979;29:47–65.

[2] Potyondy DO, Cundall PA. A bonded-particle model for rock. International Journal of Rock Mechanics and Mining Sciences 2004;41:1329–64.

[3] Cil MB, Alshibli KA. 3D assessment of fracture of sand particles using discrete element method. Géotechnique Letters 2012;2:161–6.

[4] Lobo-Guerrero S, Vallejo LE. Influence of pile shape and pile interaction on the crushable behavior of granular materials around driven piles: DEM analyses. Granular Matter 2007;9:241–50.

[5] Falagush O, McDowell GR, Yu HS, de Bono JP. Discrete element modelling and cavity expansion of cone penetration testing. Granular Matter 2015;27:483–95.

[6] Tran QA, Chevalier B, Breul P. Discrete modeling of penetration tests in constant velocity and impact conditions. Computers and Geotechnics 2016;71:12–8.

[7] LIGGGHTS . Open source discrete element method particle simulation code. 2016. URL: http://www.cfdem.com; [Cited 2016-10-18].

[8] Pingle SM, Fleck NA, Wadley HNG, Deshpande V. Discrete modeling of penetration tests in constant velocity and impact conditions. International Journal of Impact Engineering 2012;45:74–89.

[9] EDEM . Discrete element method software. 2016. URL: http://www.edemsimulation.com; [Cited 2016-10-18].

[10] Uehara JS, Ambroso MA, Ojha RP, Durian DJ. Low-speed impact craters in loose granular media. Physical Review Letters 2003;90:194301 1–4.

[11] Tsimring LS, Volfson D. Modeling of impact cratering in granular media. In: Garca-Rojo R, Herrmann HJ, McNamara S, editors. Powders and Grains; vol. 2. Rotterdam: A.A. Balkema; 2005, p. 1215–23.

[12] Seguin A, Bertho Y, Gondret P, Crassous J. Sphere penetration by impact in a granular medium: A collisional process. Europhysics Letters 2009;88:44002 1–6.

[13] Clark AH, Kondic L, Behringer RP. Particle scale dynamics in granular impact. Physical Review Letters 2012;109:238302 1–5.

[14] Nordstrom KN, Lim E, Harrington M, Losert W. Granular dynamics during impact. Physical Review Letters 2014;112:228002 1–5.

[15] Iskander M, Bless S, Omidvar M. Rapid penetration into granular media. 1st ed.; Amsterdam, Netherlands: Elsevier Inc.; 2015.

[16] Braslau D. Partitioning of energy in hypervelocity impact against loose sand target. Journal of Geophysical Research 1970;75:3987–99.

[17] Lammi CJ, Vogler TJ. Mesoscale simulations of granular materials with peridynamics. In: Elert ML, Buttler WT, Borg JP, Jordan J, Vogler TJ, editors. Shock Compression and Condensed Matter 2011: Proceedings of the Conference of the American Physical Society Topical Group on Shock Compression of Condensed Matter. AIP Publishing; 2012, p. 1467–70.

[18] Borg JP, Vogler TJ. Rapid compaction of granular material: characterizing two- and three-dimensional mesoscale simulations. Shock Waves 2013;23:153–76.

[19] Parab ND, Claus B, Hudspeth MC, Black JT, Mondal A, Sun J, et al. Experimental assessment of fracture of individual sand particles at different loading rates. International Journal of Impact Engineering 2014;68:8–14.

[20] Omidvar M, Iskander M, Bless S. Soil-projectile interactions during low velocity penetration. International Journal of Impact Engineering 2016;93:211–21.

[21] Katsuragi H, Durian DJ. Unified force law for granular impact cratering. Nature Physics 2007;3:420–3.

[22] Katsuragi H, Durian DJ. Drag force scaling for penetration into granular media. Physical Review E 2013;87:052208 1–5.

[23] Takita H, Sumita I. Low-velocity impact cratering experiments in a wet sand target. Physical Review E 2013;88:022203 1–10.

[24] Wada K, Senshu H, Matsui T. Numerical simulation of impact cratering on granular material. Icarus 2006;180:528–45.

[25] Pournaghiazar M, Russell A, Khalili N. Linking cone penetration resistances measured in calibration chambers and the field. Géotechnique Letters 2012;2:29–35.

[26] Forrestal MJ, Luk VK. Penetration into soil targets. International Journal of Impact Engineering 1992;12:427–44.

[27] Omidvar M, Iskander M, Bless S. Response of granular media to rapid penetration. International Journal of Impact Engineering 2014;66:60–82.

[28] Paik K, Salgado R, Lee J, Kim B. Behavior of open- and closed-ended piles driven into sands. Journal of Geotechnical and Geoenvironmental Engineering 2003;129:296–306.

[29] Ko J, Jeong S, Lee JK. Large deformation FE analysis of driven steel pipe piles with soil plugging. Computers and Geotechnics 2016;71:82–97.

[30] IMPETUS Afea AS . IMPETUS Afea Solver. 2016. URL: http://www.impetus-afea.com; [Cited 2016-10-18].

[31] Olovsson L. Corpuscular method for airbag deployment simulations in LS-DYNA. 2007. IMPETUS Afea AB, Huddinge (ISBN 978-82-997587-0-3).

[32] Olovsson L, Hanssen AG, Børvik T, Langseth M. A particle-based approach to close-range blast loading. European Journal of Mechanics A/Solids 2010;29:1–6.

[33] Børvik T, Olovsson L, Hanssen AG, Dharmasena KP, Hansson E, Wadley HNG. A discrete particle approach to simulate the combined effect of blast and sand impact loading of steel plates. Journal of the Mechanics and Physics of Solids 2011;59:950–8.

[34] Wadley HNG, Børvik T, Olovsson L, Wetzel JJ, Dharmasena KP, Hopperstad OS, et al. Deformation and fracture of impulsively loaded sandwich panels. Journal of the Mechanics and Physics of Solids 2013;61:674–99.

[35] Holloman RL, Deshpande V, Wadley HNG. Impulse transfer during sand impact with a solid block. International Journal of Impact Engineering 2015;76:98–117.

[36] Holloman RL, Deshpande V, Wadley HNG. Impulse transfer during sand impact with a cellular structure. International

Journal of Impact Engineering 2015;82:36–58.

[37] Børvik T, Dey S, Olovsson L. Penetration of granular materials by small-arms bullets. International Journal of Impact Engineering 2015;75:123–39.

[38] Holmen JK, Hopperstad OS, Børvik T. Experiments and simulations of empty and sand-filled aluminum alloy panels subjected to ballistic impact. Engineering Structures 2017;130:216–28.

[39] Moxnes JF, Frøyland Ø, Skriudalen S, Prytz AK, Teland JA, Friis E, et al. On the study of ricochet and penetration in sand, water and gelatin by spheres, 7.62 mm, and 25 mm projectiles. Defence Technology 2016;12:159–70.

[40] Bjerke FR, Hansen LM. Experimental and numerical study on the perforation of empty and sand-filled aluminium panels. Master's thesis; Norwegian University of Science and Technology (NTNU); 2015.

[41] Deshpande VS, McMeeking RM, Wadley HNG, Evans AG. Constitutive model for predicting dynamic interactions between soil ejecta and structural panels. Journal of the Mechanics and Physics of Solids 2009;57:1139–64.

[42] Goldman DI, Umbanhowar P. Scaling and dynamics of sphere and disk impact into granular media. Physical Review E 2008;77:021308 1–14.

[43] Kondic L, Fang X, Losert W, O'Hern CS, Behringer RP. Microstructure evolution during impact on granular matter. Physical Review E 2012;85:011305 1–17.